

Fundamental mechanisms of the growth and decay of the PNA teleconnection pattern

By STEVEN B. FELDSTEIN*
The Pennsylvania State University, USA

(Received 11 December 2000; revised 24 October 2001)

SUMMARY

This investigation performs diagnostic analyses on NCEP/NCAR re-analysis data, and also does forced, nonlinear, barotropic model calculations to examine the dynamical mechanisms associated with the growth and decay of the Pacific/North American teleconnection pattern (PNA). The diagnostic calculations include projection and composite analyses of each term in the stream-function-tendency equation.

The results of the diagnostic analyses and model calculations reveal a PNA life cycle that is complete within approximately 2 weeks and is dominated by linear processes. The growth of the two upstream PNA anomaly centres is found to be by barotropic conversion from the zonally asymmetric climatological flow, and the two downstream PNA anomaly centres by linear dispersion. The PNA anomaly growth eventually ceases because of changes in the spatial structure of the anomaly. An analysis of the role of Ekman pumping is performed with a very simple model. The results, although qualitative, suggest that the decay of the PNA may be through Ekman pumping. An examination of the role of transient eddy vorticity fluxes indicates that they play an important role during some stages of the PNA life cycle. Lastly, the model calculations also reveal a crucial role played by the divergence term in maintaining the PNA anomaly in a quasi-fixed position.

KEYWORDS: Low-frequency variability Teleconnection patterns

1. INTRODUCTION

The results of two recent observational studies suggest that the Pacific/North American teleconnection pattern (hereafter PNA) undergoes a life cycle of growth and decay within a time span of about 2 weeks (Feldstein 2000; Cash and Lee 2001). Feldstein (2000) examined the power spectral properties of a number of different teleconnection patterns. For the PNA, it was found that the power spectrum of the daily unfiltered principal component (PC) time series closely matched that of a first-order Markov (red noise) process with a decorrelation time-scale of 7.7 days. (The decorrelation time-scale is defined to be the time it takes for the autocorrelation function of a first-order Markov process to decay by a factor of e .) Consistently, Cash and Lee (2001) showed with a linear multivariate stochastic model that the PNA is the most probable spatial pattern to evolve from the first optimal perturbation. In fact, they found this property to be very robust, as more than 70% of the observed PNA events were found to arise from this process. In addition, Cash and Lee (2001), and also the idealized modelling study of Franzke *et al.* (2001), showed that the PNA anomaly completes its life cycle of growth and decay within about 2 weeks.

A number of different theories have been proposed that may account for the growth and maintenance of low-frequency anomalies, such as the PNA. These include: (i) barotropic growth due to the zonal asymmetry of the climatological flow (e.g. Fredriksen 1983; Simmons *et al.* 1983; Branstator 1990, 1992), (ii) growth due to linear dispersion from a source of topographic or diabatic heating (e.g. Hoskins and Karoly 1981), (iii) a combined baroclinic/barotropic instability or initial-value development (e.g. Dole and Black 1990; Black and Dole 1993), (iv) changes in quasi-stationary eddies due to zonal mean-flow fluctuations (e.g. Branstator 1984; Nigam and Lindzen 1989; Kang 1990), and (v) feedback by high-frequency transient eddy fluxes (e.g. Egger and Schilling 1983; Lau 1988; Branstator 1992; Ting and Lau 1993).

* Corresponding address: EMS Environment Institute, The Pennsylvania State University, University Park, PA 16802, USA. e-mail: sbf@essc.psu.edu

The present study examines the dynamical processes associated with the temporal evolution of the PNA. The approach adopted includes an examination of the composite temporal evolution of each term in the stream-function-tendency equation (the inverse Laplacian of the vorticity equation) during the PNA life cycle. With this approach, which will be complemented by both linear and nonlinear barotropic model calculations, it will be possible to isolate which dynamical process account for both the growth and the decay of the PNA.

In section 2 the data and diagnostic techniques are described. This is followed in section 3 by an examination of the spatial structure of the PNA. The temporal evolution of the PNA is briefly described in section 4, followed by a projection analysis in section 5. The results from the composite stream-function-tendency equation are presented in section 6, followed by barotropic model calculations in section 7. The conclusions are given in section 8.

2. DATA AND DIAGNOSTIC TECHNIQUES

The daily (00 UTC) 300 mb stream-function field is used. This quantity is obtained by logarithmic interpolation from the daily (00 UTC) National Centers for Environmental Prediction/National Center for Atmospheric Research (NCEP/NCAR) re-analysis vorticity field in sigma coordinates (where sigma equals pressure divided by surface pressure). These data cover the years from 1979 to 1995 for the months of November to March. The seasonal cycle is removed at each grid point. The seasonal cycle is obtained by taking the calendar mean for each day and applying a 20-day low-pass digital filter. All data used in this study are at rhomboidal 30 resolution. The PNA is identified by applying a rotated principal component analysis (RPCA) with a varimax rotation to the data. As the covariance matrix is used, the corresponding PC time series (in this study, the PC time series will also be referred to as the PNA index time series) is orthonormal.

A 31-point, 10-day, low-pass digital filter is applied to the stream-function-tendency equation. The effect of using this filter is simply to smooth the temporal evolution of each term in the stream-function-tendency equation, slightly, without altering the interpretation. As shown by Feldstein (1998), the influence of this particular filter is negligible for anomalies which grow or decay within a time period as short as 5 days. Furthermore, the same 10-day cut-off is used to distinguish between low- and high-frequency transient eddies. Although to a large degree this cut-off frequency is arbitrary, it is selected because eddy fluxes on either side of this cut-off frequency tend to yield different structural properties (Hoskins *et al.* 1983).

(a) Definitions

Persistent episodes are defined using an objective method adopted from Horel (1985) and Mo (1986) (see also Feldstein 1998). A pattern correlation r at day t and lag τ is defined as

$$r(t, \tau) = \frac{\langle \psi'(\lambda, \theta, t) \psi'(\lambda, \theta, t + \tau) \rangle}{\sigma\{\psi'(\lambda, \theta, t)\} \sigma\{\psi'(\lambda, \theta, t + \tau)\}}, \quad (1)$$

where $\psi(\lambda, \theta, t)$ is the anomalous (deviation from the seasonal cycle) stream function at longitude λ and latitude θ , and $\psi' = \psi(\lambda, \theta, t) - \langle \psi(\lambda, \theta, t) \rangle$, $\sigma^2\{\psi'(\lambda, \theta, t)\} = \langle \{\psi'(\lambda, \theta, t)\}^2 \rangle$, where the angle brackets denote a horizontal average over the northern hemisphere. If both $r(t, \tau)$ and $r(t + 1, \tau) \geq r_c$, for $\tau = 1$ to 5 days, a persistent episode is defined to have taken place. For this study, a value of $r_c = 0.254$ is used, which

corresponds to the 95% confidence level. The number of degrees of freedom is obtained from the Fisher Z-transformation (see Feldstein and Lee 1996). For each persistent episode, an onset day is defined to correspond to the first day of the persistent episode. One additional requirement is imposed on the definition of a persistent episode. This is that the magnitude of the PC for the PNA exceeds one standard deviation on the onset day. Also, when the PC is positive (negative) during a persistent episode, that episode will be referred to as corresponding to the positive (negative) phase. Furthermore, if the onset day of one persistent episode takes place within 15 days of the end of the previous persistent episode, and if both episodes are of the same phase, then the latter persistent episode is discarded. Using this definition, it is found that there are 26 (29) persistent episodes for the positive (negative) phase.

(b) *Stream-function-tendency equation*

The primary technique used in this study is a composite analysis of each term in the stream-function-tendency equation (Cai and van den Dool 1994; Feldstein 1998), which can be written as

$$\frac{\partial \psi^L}{\partial t} = \sum_{i=1}^8 \xi_i + R, \quad (2)$$

where

$$\begin{aligned} \xi_1 &= \nabla^{-2} \left(-(v_r^L + v_d^L) \frac{1}{a} \frac{df}{d\theta} \right) \\ \xi_2 &= \nabla^{-2} (-[\bar{\mathbf{v}}_r] \cdot \nabla \zeta^L - \mathbf{v}_r^L \cdot \nabla [\bar{\zeta}]) + \nabla^{-2} (-[\bar{\mathbf{v}}_d] \cdot \nabla \zeta^L - \mathbf{v}_d^L \cdot \nabla [\bar{\zeta}]) \\ \xi_3 &= \nabla^{-2} (-\bar{\mathbf{v}}_r^* \cdot \nabla \zeta^L - \mathbf{v}_r^L \cdot \nabla \bar{\zeta}^*) + \nabla^{-2} (-\bar{\mathbf{v}}_d^* \cdot \nabla \zeta^L - \mathbf{v}_d^L \cdot \nabla \bar{\zeta}^*) \\ \xi_4 &= \nabla^{-2} \{ -(f + \bar{\zeta}) \nabla \cdot \mathbf{v}_d^L - \zeta^L \nabla \cdot \bar{\mathbf{v}}_d \} \\ \xi_5 &= \nabla^{-2} (-\mathbf{v}_r^L \cdot \nabla \zeta^L)^L + \nabla^{-2} \{ -\nabla \cdot (\mathbf{v}_d^L \zeta^L) \}^L \\ \xi_6 &= \nabla^{-2} (-\mathbf{v}_r^H \cdot \nabla \zeta^H)^L + \nabla^{-2} \{ -\nabla \cdot (\mathbf{v}_d^H \zeta^H) \}^L \\ \xi_7 &= \nabla^{-2} (-\mathbf{v}_r^L \cdot \nabla \zeta^H)^L + \nabla^{-2} \{ -\nabla \cdot (\mathbf{v}_d^L \zeta^H) \}^L + \nabla^{-2} (-\mathbf{v}_r^H \cdot \nabla \zeta^L)^L \\ &\quad + \nabla^{-2} \{ -\nabla \cdot (\mathbf{v}_d^H \zeta^L) \}^L \\ \xi_8 &= \nabla^{-2} \{ -\mathbf{k} \cdot \nabla \times (\omega^L \partial \bar{\mathbf{v}} / \partial p) \} + \nabla^{-2} \{ -\mathbf{k} \cdot \nabla \times (\bar{\omega} \partial \mathbf{v}^L / \partial p) \} \\ &\quad + \nabla^{-2} \{ -\mathbf{k} \cdot \nabla \times (\omega' \partial \mathbf{v}' / \partial p) \}^L, \end{aligned}$$

and ψ is the stream function, ζ the relative vorticity, \mathbf{v} the horizontal wind vector, v the meridional wind component, ω the vertical wind component, a the earth's radius, p the pressure, \mathbf{k} the unit vector in the vertical direction, and f the Coriolis parameter. The term R corresponds to a residual, and includes physical processes that have been neglected such as frictional dissipation. The subscripts 'r' and 'd' represent the rotational and divergent components of the horizontal wind, respectively, and the superscripts 'L' and 'H' indicate the application of the 10-day low-pass and high-pass filter, respectively. For the low-pass filter, the 1979–1995 November to March time mean is also subtracted. An overbar denotes a time mean, a prime a deviation from the time mean, square brackets a zonal average, and an asterisk a deviation from the zonal average. Standard definitions are used for all remaining terms. The term $\partial \psi^L / \partial t$ is calculated using centred time differences. One important property of (2) is that although this equation describes

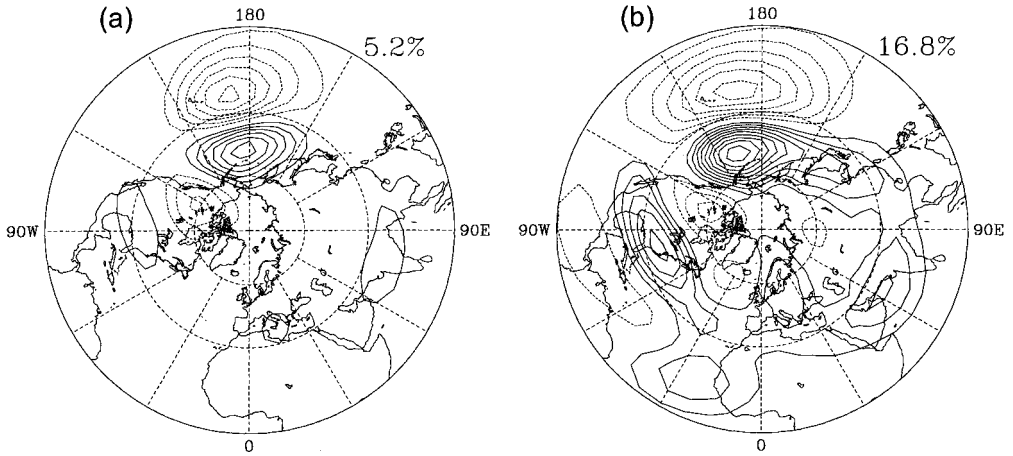


Figure 1. The (a) unified daily, and (b) monthly averaged first rotated empirical orthogonal function, that corresponds to the Pacific/North American teleconnection pattern. The fractional variance is shown in the upper right corner of each frame. Dashed contours are negative, and the zero contour is omitted.

the low-frequency evolution of the stream-function anomaly, it indicates that part of the low-frequency stream function is driven by anomalous eddy fluxes associated with high-frequency transients.

As discussed by Feldstein (1998), ξ_1 involves planetary vorticity advection by the anomaly, ξ_2 (ξ_3) the interaction of the anomaly with the zonal mean (zonally asymmetric) climatological flow, and ξ_4 the divergence term. The term ξ_5 corresponds to the interaction amongst all low-frequency transient eddies, and ξ_6 to the forcing by high-frequency transient eddies. Also, as shown by Feldstein (1998), the terms ξ_7 and ξ_8 , which correspond to the anomalous cross-frequency vorticity flux and tilting terms, make a negligible contribution to the stream-function tendency. Thus, these two terms will not be considered in the remainder of this study.

3. PNA SPATIAL STRUCTURE

The first rotated empirical orthogonal function (REOF1) from the daily, unfiltered 300 mb stream-function field is shown in Fig. 1(a). The quadrupole pattern seen is typical for a PNA pattern, with centres over the subtropical Pacific near Hawaii, south of the Aleutian Islands, north-western Canada, and the south-eastern United States (e.g. Wallace and Gutzler 1981). (It should be noted that there is no prominent pattern that is in quadrature with REOF1. This indicates that REOF1 corresponds to a stationary, not a propagating, pattern.) Most studies of the PNA use either monthly or seasonal averaged data. Thus, with the same dataset, an RPCA is performed on the monthly averaged 300 mb stream-function field (Fig. 1(b)). As can be seen, the two patterns are very similar, the most noticeable differences being the larger zonal scale and the two relatively stronger downstream centres in the monthly-averaged data. For each of these calculations, 12 unrotated EOFs were retained. Both the illustrated spatial patterns, and the corresponding PC time series, were found to be rather insensitive to the number of retained unrotated EOFs, when tested over a range of between 10 and 20 unrotated EOFs.

In order to test the similarity quantitatively between the two REOF1 patterns in Fig. 1, the following procedure is adopted. First, the daily PC time series is taken and

a new time series is generated consisting of monthly averages. This time series is then correlated with the monthly PC time series. Such a calculation yields a linear correlation of 0.83. As a measure that the REOFs in Fig. 1 do indeed correspond to PNA patterns found in other studies, the monthly PC time series for REOF1 was correlated with the monthly PNA index made available from the Climate Prediction Center, for the same set of 85 winter months as in the present study. The linear correlation was found to be 0.84. Given that the Climate Prediction Center follows a different methodology, e.g. applies the RPCA to a different pressure level, i.e. 700 mb, and uses a different variable, i.e. geopotential height, this large linear correlation does give one confidence that the two REOFs in Fig. 1 do indeed correspond to a PNA.

It is important to emphasize that the precise location or phase of each of the four anomaly centres of the PNA is not very robust. For example, amongst the numerous papers that have been published on the PNA, using different methodologies and datasets, a range of patterns have appeared that are collectively referred to as the PNA. The common feature to most of these so-called PNA patterns is that there is a wave train with two anomaly centres over the North Pacific and two over North America, as in Fig. 1. However, the precise location of these individual anomaly centres varies from one study to the next. Even within the same dataset, as shown in the rotated EOF analysis of Kushnir and Wallace (1989), the exact location of the four PNA anomaly centres is sensitive to the type of rotation used. Thus, there is no single spatial pattern that can be referred to as *the* PNA, since the geographic location of all four anomaly centres is not unique. As a result, it seems best to refer to all those patterns with the above characteristics as being PNA-like patterns. In the context of the present study, this implies that we are examining the properties of one particular PNA-like pattern, i.e. the pattern obtained through a varimax rotation, the most popular method of rotation used in studies of low-frequency variability. (In this study, when the term PNA is used, it is important to note that it is the patterns in Fig. 1 that are being referred to, and not to all PNA-like patterns). Nevertheless, given the similarity of all PNA patterns, it is anticipated that the results of this study would at least apply *qualitatively* to all PNA-like patterns. However, a sensitivity analysis for a range of PNA-like patterns is beyond the scope of this study.

It is also important to state that since the winter season is defined to include five different months, this study is overlooking the property that teleconnection patterns such as the PNA undergo some seasonal variation (Barnston and Livezey 1987). However, such a lengthy winter season was chosen so as to include all onset days within the months of December to February, while allowing for an examination of lagged fields that extend ± 20 days into November and March.

4. TEMPORAL EVOLUTION OF THE PNA

The temporal evolution of the PNA can be succinctly described by examining composites of the PNA index (Fig. 2(a) for the positive phase and Fig. 3(a) for the negative phase). As can be seen, for both phases, the PNA index grows and decays rapidly, completing most of its life cycle within approximately 15 days. One noticeable difference between the two phases, however, is that for the negative phase the PNA index remains at about 30% of its peak value for about 10 days after undergoing substantial decline. This point is discussed in more detail in section 6. The temporal evolution of the anomalous composite 300 mb stream-function field for the positive phase (the negative phase shows similar characteristics) is illustrated in Fig. 4. As a measure of local statistical significance, the corresponding *t*-values that exceed the 95% confidence

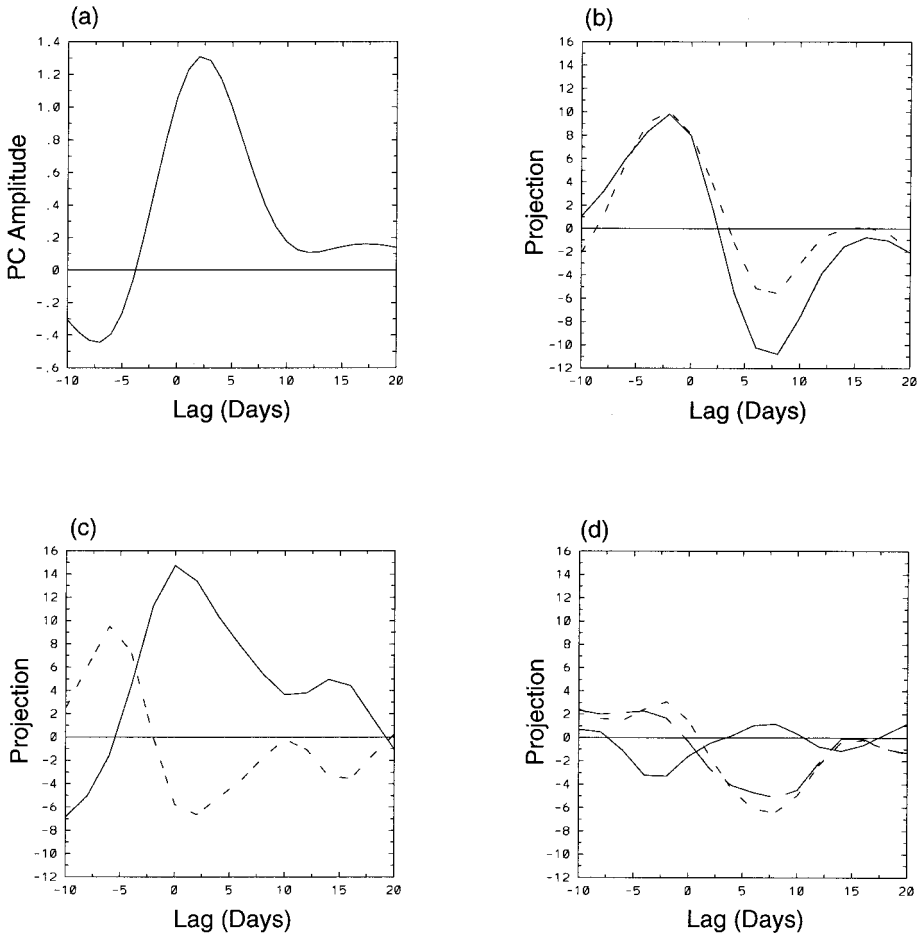


Figure 2. (a) Composite time series of the Pacific/North American teleconnection pattern index for the positive phase. Time-lagged projections of the following combinations of terms onto the daily unfiltered first rotated empirical orthogonal function: (b) $\sum_{i=1}^8 \xi_i$ (full line), $\sum_{i=1}^4 \xi_i$ (dashed line); (c) ξ_3 (full line), ξ_4 (dashed line); (d) ξ_6 (full line), ξ_5 (short-dashed line), incoherent eddy contribution to ξ_5 (long-dashed line). The units for the ordinate in each frame are arbitrary. See text for explanation of terms.

level for a two-sided t -test are shown with shading in Fig. 4. At 4 days before onset (Fig. 4(a)), the four centres associated with the PNA are already present. However, as the two upstream centres are located about 30° east of the corresponding centres in REOF1 (see Fig. 1(a)), the composite PNA index remains small at this lag. By onset (Fig. 4(b)), the two upstream centres have moved westward toward the Asian jet and the entire pattern has amplified. The PNA spatial pattern is maintained through 4 days after onset (Fig. 4(c)) (the maximum-amplitude anomaly occurs at lag +2 days), after which rapid decay takes place (Fig. 4(d)). Also, the signal of the Kushnir–Branstator mode (Branstator 1987; Kushnir 1987) seems to be present in Fig. 4. One of the features of the Kushnir–Branstator mode is westward anomaly propagation over North America and the North Pacific. An examination of Figs. 5(c) and 5(d) of Branstator (1987) shows westward propagation of negative stream-function anomalies over North America and the subtropical Pacific and also westward propagation of a positive stream-function anomaly off the west coast of North America. These same features are seen between

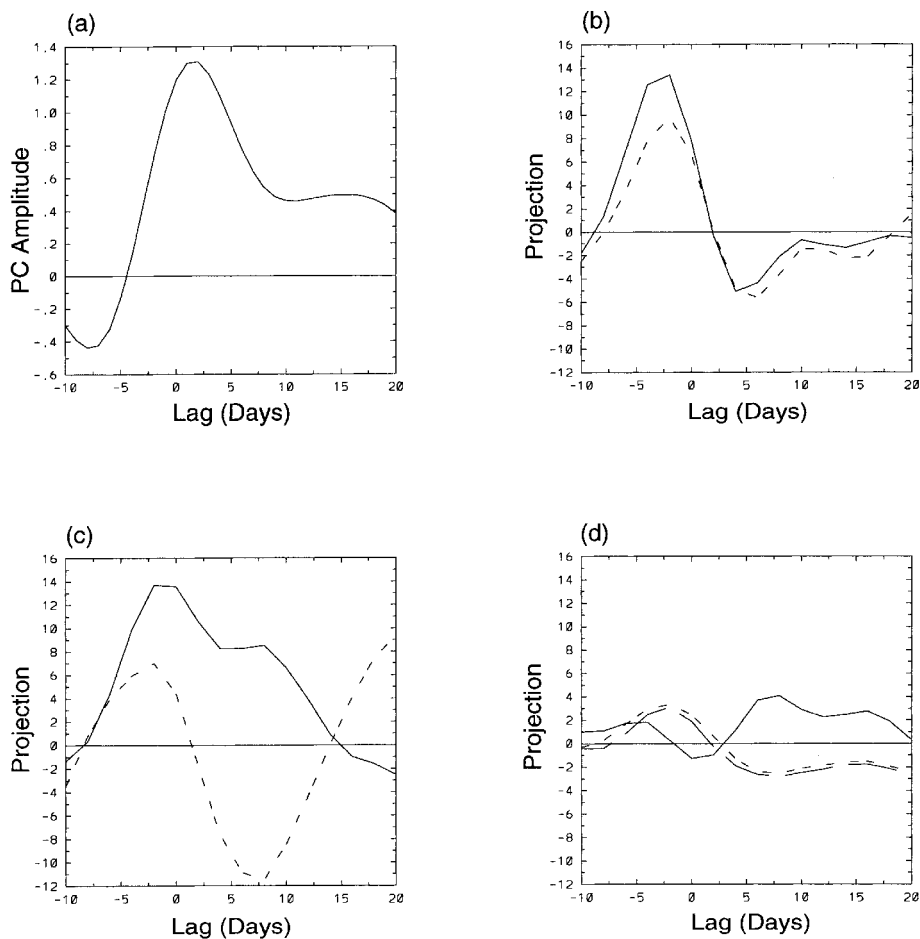


Figure 3. As for Fig. 2, except for the negative phase. In order to compare Figs. 2 and 3, the signs of each curve in Fig. 3 have been changed.

lag -4 days and onset in Fig. 4. This suggests that the initial development of the PNA may be associated with the Kushnir–Branstator mode.

The global field significance (Livezey and Chen 1983) of the patterns in Fig. 4 was also examined. A series of 1000 Monte Carlo composite patterns was first obtained in which the onset days were selected randomly. It was found that 5% of these patterns had more than 8.6% of their area exceed the 95% confidence level for a 2-sided t -test. As all four frames in Fig. 4 were found to have greater than 8.6% of their area exceed the above requirements for a t -test (for Figs. 4(a), 4(b), 4(c), and 4(d), 15.2%, 30.0%, 22.5%, and 10.0%, respectively, of the area was found to exceed the 95% confidence level for a 2-sided t -test), each of the spatial patterns in Fig. 4 does indeed pass the field significance test at the 95% confidence level.

5. PROJECTIONS

In order to summarize the role of each term on the right-hand side (r.h.s.) of (2), we project each of these terms onto the REOF1 spatial pattern. The projection, P_i , can be

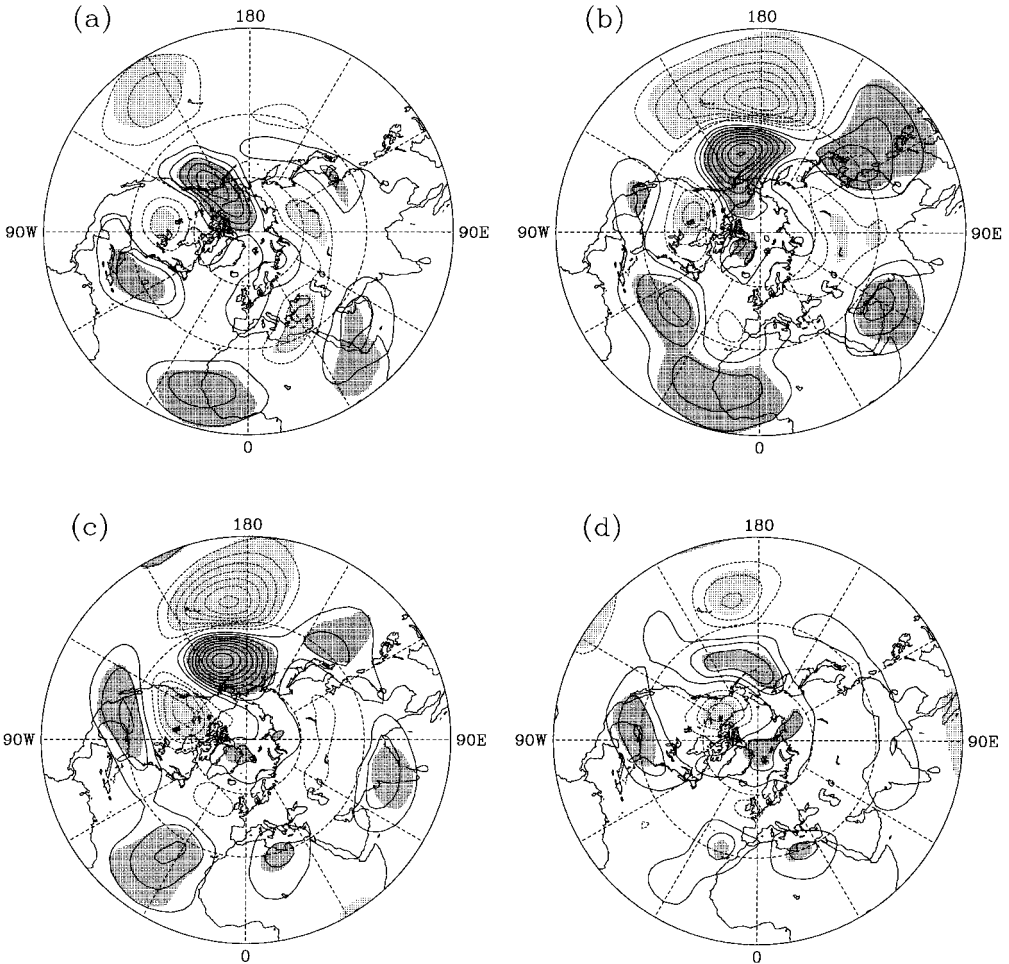


Figure 4. Composites of the anomalous 300 mb stream-function field at (a) lag -4 days, (b) lag 0 days, (c) lag $+4$ days, and (d) lag $+8$ days. Contour interval is $2 \times 10^6 \text{ m}^2 \text{ s}^{-1}$. Dashed contours are negative, and the zero contour is omitted. Dense (light) stippling indicates positive (negative) t -values that exceed the 95% confidence level.

written as

$$P_i = \sum_j \xi_{ij}(\lambda, \theta) r_{1j}(\lambda, \theta) \cos^{1/2} \theta, \quad (3)$$

where ξ_{ij} is the i th term on the r.h.s. of (2) and r_{1j} is the REOF1, both expressed at the j th grid point. The summation in (3) extends over all grid points in the northern hemisphere.

In order to illustrate the meaning of this projection, we examine the equation obtained by projecting both sides of (2) onto REOF1. We began by noting that for sufficiently large N , the stream-function field can be written as

$$\psi^L \simeq \sum_{n=1}^N a_n(t) r_n(\lambda, \theta) / \cos^{1/2} \theta, \quad (4)$$

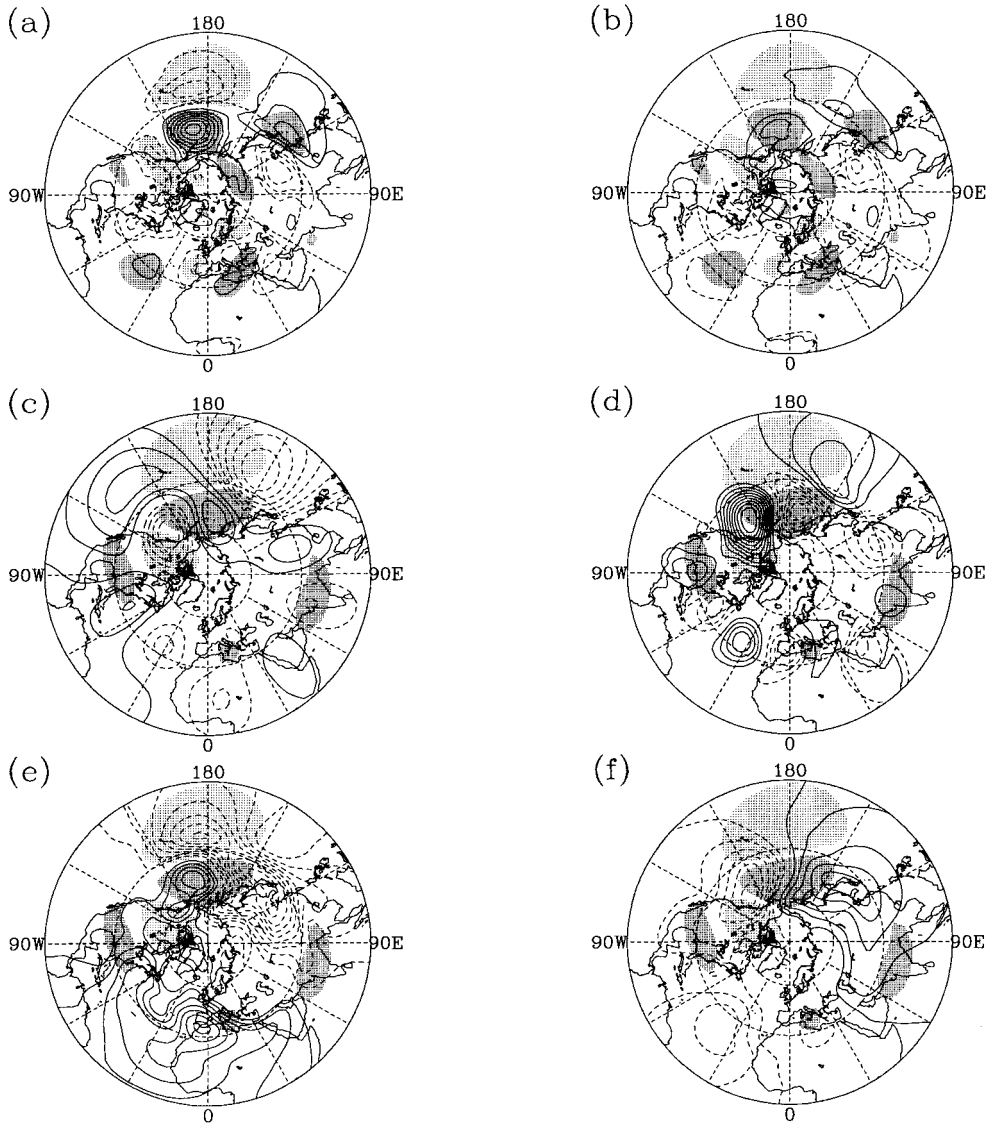


Figure 5. Composites at lag -2 days of various combinations of terms on the right-hand side (r.h.s.) of Eq. (2): (a) the sum of all terms on the r.h.s. of (2), $\sum_{i=1}^8 \xi_i$, (b) the residual R , (c) ξ_1 , (d) ξ_2 , (e) ξ_3 , and (f) ξ_4 (see text). The contour interval is $10.0 \text{ m}^2 \text{ s}^{-2}$ in (a), (b), and (e) and is $25.0 \text{ m}^2 \text{ s}^{-2}$ in (c), (d) and (f). Dashed contours are negative, and the zero contour is omitted. Dense (light) stippling indicates positive (negative) values of the anomalous 300 mb stream-function tendency in (a) and (b), and the daily unfiltered first rotated empirical orthogonal function in (c) to (f). The stippling is above a magnitude of $10.0 \text{ m}^2 \text{ s}^{-2}$ in (a) and (b).

where a_n and r_n are the n th PC time series and n th REOF, respectively. As discussed in section 3, the number of rotated EOFs, N , is set at $N = 12$. Substituting (4) into (2) and neglecting the residual yields

$$\sum_{n=1}^N \frac{da_n}{dt} r_n / \cos^{1/2} \theta = \sum_{i=1}^8 \xi_i. \quad (5)$$

Multiplying (5) by $r_1 \cos^{1/2} \theta$ and integrating over the domain results in

$$\frac{da_1}{dt} \sum_j r_1^2 + \frac{da_2}{dt} \sum_j r_1 r_2 + \cdots + \frac{da_{12}}{dt} \sum_j r_1 r_{12} = \sum_{i=1}^8 \sum_j r_1 \xi_i \cos^{1/2} \theta. \quad (6)$$

All $N = 12$ terms on the left-hand side (l.h.s.) of (6) have nonzero values, which is a manifestation of the nonorthogonality of rotated EOFs. However, a calculation of each term on the l.h.s. of (6) reveals that the first term is more than 25 times larger than each of the other terms at most lags during the persistent episode. In fact, neglecting all but the first term on the l.h.s. of (6) is found to yield an error in the value of da_1/dt which is of the order of 10%. Thus, to an excellent approximation, the projection in (3) represents the influence of individual ξ_i on the rate of change with time of the PNA index.

The various projections for the positive phase are examined in Fig. 2, and for the negative phase in Fig. 3. A comparison between the projection of the sum of 'linear' terms, i.e. $\sum_{i=1}^4 \xi_i$ and that for all the terms $\sum_{i=1}^8 \xi_i$ (Figs. 2(b) and 3(b)) indicates that the linear terms play a crucial role during both the growth and the decay of the PNA anomaly. For example, during the positive phase (Fig. 2(b)), the linear terms account for essentially all of the anomaly growth and about one half of the anomaly decay. For the negative phase (Fig. 3(b)), on the other hand, the linear terms account for about two thirds of the anomaly growth, and most of the anomaly decay. A close examination of each of the first four ξ_i terms shows for both phases that the PNA growth is dominated by ξ_3 (Figs. 2(c) and 3(c)). This term, referred to as stationary advection by Feldstein (1998), involves an energy transfer from the climatological stationary eddies to the anomaly (e.g. Frederiksen 1983; Simmons *et al.* 1983; Branstator 1990, 1992). Furthermore, for both phases, it is found that during the anomaly decay it is the divergence term, ξ_4 , that dominates the first four ξ_i terms (Figs. 2(c) and 3(c)). Also, the projections by the 'nonlinear' terms ξ_5 and ξ_6 (Figs. 2(d) and 3(d)), i.e. the low- and high-frequency transient eddy fluxes, reveal that ξ_5 and ξ_6 tend to oppose one another at most lags. This cancellation between the two bands of transient eddy fluxes lowers the role played by transient eddy fluxes during the PNA life cycle. Therefore, because the projections during the growth (decay) stage are dominated by ξ_3 (ξ_4), the results of this projection analysis suggest that the composite PNA anomaly can be described as undergoing a life cycle dominated by linear growth and linear decay. The growth is primarily through stationary advection and the decay through divergence.

It is also important to discuss some of the potential drawbacks of the projection technique. Firstly, the projection is onto a stationary anomaly pattern, i.e. REOF1. The advantage of this type of projection, as discussed earlier, is that it allows for an unambiguous estimate of the influence of the terms on the r.h.s. of (2) on the PC tendency. Furthermore, when the stream-function anomaly is quasi-stationary and resembles REOF1, such as between lags 0 and lag +8 days (see Figs. 4(b) to 4(d)) it is anticipated that the projections onto REOF1 also determine which terms on the r.h.s. of (2) affect the instantaneous stream-function anomaly. However, if the stream-function anomaly undergoes substantial propagation, as is evident at negative lags in Fig. 4, the projections onto REOF1 still describe the influence of the terms on the r.h.s. of (2) on the PC tendency, but are no longer accurate at describing the influence of these terms on the instantaneous stream-function anomaly.

In order to quantify the limitations of projecting onto REOF1, the projections onto REOF1 are compared with those onto the instantaneous stream-function-anomaly pattern. The latter projection is a measure of the extent to which terms on the r.h.s. of (2) influence the temporal evolution of the instantaneous stream-function anomaly.

As expected, the two types of projections were found to be similar primarily during the persistent episode (for a definition of persistent episode, see subsection 2(a)), and also for up to 2 days before the onset day (not shown). During this time period, the differences between the two types of projections were less than 30% at most lags. On the other hand, at earlier lags, when the stream-function-anomaly propagation is most pronounced, larger differences between the two types of projections were found. Amongst the differences noted, it was found that the projection onto the instantaneous stream-function anomaly indicated an initiation of anomaly growth about 4 days earlier than that shown in Figs. 2 and 3. Such a result is to be expected when the stream-function anomaly propagates. Also, between lag -10 and lag -5 days, it is found that the projection by the sum of the high- and low-frequency transient eddy fluxes is about twice that by the stationary advection term. This suggests that at the earliest stage of the anomaly evolution, the initial disturbance, which grows east of the PNA region, is excited by transient eddy fluxes. Such a result appears to be consistent with Dole and Black (1990) and Black and Dole (1993) who find that baroclinic processes are important during the growth of North Pacific low-frequency anomalies.

Another potential limitation involves the property that the projection encompasses the entire northern hemisphere. It is plausible that small local contributions to the projections from locations where the anomaly is weak could make a significant contribution to the hemispherically integrated projections illustrated in Figs. 2 and 3. To address this question, projections corresponding to those shown in Figs. 2 and 3 were re-calculated for a domain confined between 150°E , 60°W , the equator, and the north pole. This domain encompasses the four main centres of the PNA anomaly illustrated in Fig. 1. The results of this calculation revealed only small changes for the projections associated with stationary advection and the high- and low-frequency transient eddy fluxes, i.e. at most lags the difference between the full projection and that confined to the PNA region was less than 15%. The changes for the divergence term were somewhat larger, but not large enough to alter the dynamical interpretation, as the difference between the two types of projections was less than 35% at most lags. These results verify that all of the projections shown in Figs. 2 and 3 are dominated by the PNA anomaly.

6. STREAM-FUNCTION-TENDENCY EQUATION

The spatial structure of various terms on the r.h.s. of (2) is now illustrated. As the general characteristics are similar for both phases, this is shown only for the positive phase. First, we evaluate to what extent the budget is balanced, as there are a number of possible sources of error that are present. This includes errors from the finite-differencing schemes, interpolation from sigma onto the 300 mb pressure surface, the exclusion of the cross-frequency vorticity flux and tilting terms, and neglected physical processes such as frictional dissipation. The extent to which the budget is balanced is first examined by overlaying contours of the sum of the terms on the r.h.s. of (2) (neglecting the residual) on shading of the stream-function tendency, i.e. the l.h.s. of (2) (see Fig. 5(a)). For this purpose, lag -2 days is selected, which is close to the time when the PNA index is increasing most rapidly. As can be seen, there is a very good match between the two fields at most locations, especially in the PNA region. In Fig. 5(b), the contours of the residual term are shown, also overlaying shading of the stream-function tendency. As can be seen, at most locations, and especially where the stream-function anomaly has its largest amplitude, the residual term is much smaller than the stream-function tendency, indicating that the budget is reasonably well balanced. (A similar degree of balance is found for the negative phase.)

Composites of the linear terms, i.e. ξ_1 , ξ_2 , ξ_3 , and ξ_4 , are shown in Figs. 5(c) to 5(f). These fields are illustrated with contours overlaying shading of the daily REOF1 spatial pattern. Again lag -2 days is selected, in order to illustrate the characteristics of these terms while the PNA anomaly is growing most rapidly. As is typical for a Rossby wave, the planetary (relative) vorticity advection, ξ_1 (ξ_2), acts to drive the anomalies westward (eastward). Consistent with the projection in Fig. 2(c), the spatial pattern for ξ_3 accounts for strong amplification of the stream-function anomaly. Lastly, the anomalous divergence, ξ_4 , drives the stream-function anomaly westward. Such westward propagation is consistent with the anomalous divergence corresponding to the anomalous secondary circulation induced by anomalous vorticity advection (Holton 1992). A similar relation between blocking anomalies and the divergence term was found by Cash and Lee (2000). Also, the composite of the sum of these four linear terms results in substantial cancellation (not shown). Very similar characteristics were found for the low-frequency anomaly by Feldstein (1998).

Next some of the properties of the low-frequency interaction term, ξ_5 , are examined. It is first beneficial to separate ξ_5 into a contribution solely from the composite stream-function anomaly and a contribution which does not include the composite, referred to here as ‘incoherent eddies’. This separation can be accomplished by first writing the wind and vorticity fields as $\mathbf{v}^L = \mathbf{v}_C^L + \mathbf{v}_I^L$ and $\zeta = \zeta_C^L + \zeta_I^L$, respectively, where the subscript ‘C’ denotes the composite stream-function anomaly, and the subscript ‘I’ denotes the incoherent eddy contribution. Then, the first term in ξ_5 , which involves relative vorticity advection amongst the low-frequency transients, can be rewritten without the ∇^{-2} operator as

$$(-\mathbf{v}_I^L \cdot \nabla \zeta^L)^L = (-\mathbf{v}_{rC}^L \cdot \nabla \zeta_C^L)^L + (-\mathbf{v}_{rC}^L \cdot \nabla \zeta_I^L)^L + (-\mathbf{v}_{rI}^L \cdot \nabla \zeta_C^L)^L + (-\mathbf{v}_{rI}^L \cdot \nabla \zeta_I^L)^L. \quad (7)$$

The first term on the r.h.s. of (7) is referred to as the ‘self interaction’ by the composite stream-function anomaly. The sum of the latter three terms on the r.h.s. of (7), referred to as the ‘incoherent low-frequency vorticity advection’, is dominated by $(-\mathbf{v}_{rI}^L \cdot \nabla \zeta_I^L)^L$. It should be noted that a similar separation could be applied to the second term in ξ_5 . However, as it is found that the contribution from the composite field is negligible for that term, such a separation is not made.

Before examining the spatial structure of ξ_5 , let us look at the projection made by ξ_5 with the self-interaction term being neglected (see Figs. 2(d) and 3(d)). As can be seen, this particular projection is very similar to that for ξ_5 . This implies that the self-interaction term plays a minor role and that the ξ_5 influence on the amplitude of the PNA index is primarily through the incoherent eddies.

ξ_5 and ξ_6 are illustrated at lag $+6$ days in Figs. 6(a) and 6(b), respectively. This lag corresponds to the time when the PNA is undergoing rapid decay. As can be seen, both ξ_5 and ξ_6 primarily influence the stream-function anomaly centred over the North Pacific. At earlier lags during the PNA life cycle, before the PNA index attains its maximum value at lag $+2$ days, the structure of ξ_6 is less well organized (not shown). However, beginning at lag $+4$ days and continuing through the rest of the persistent episode, ξ_6 maintains a structure resembling that shown in Fig. 6(b), with the largest projection onto the stream-function anomaly being in the North Pacific (not shown). Such behaviour is consistent with a feedback taking place by the high-frequency transient eddy fluxes after the PNA anomaly is established. The temporal evolution of ξ_5 is also rather complex. An examination of the spatial structure of ξ_5 reveals that the largest projections are always onto the North Pacific stream-function anomaly. From lag

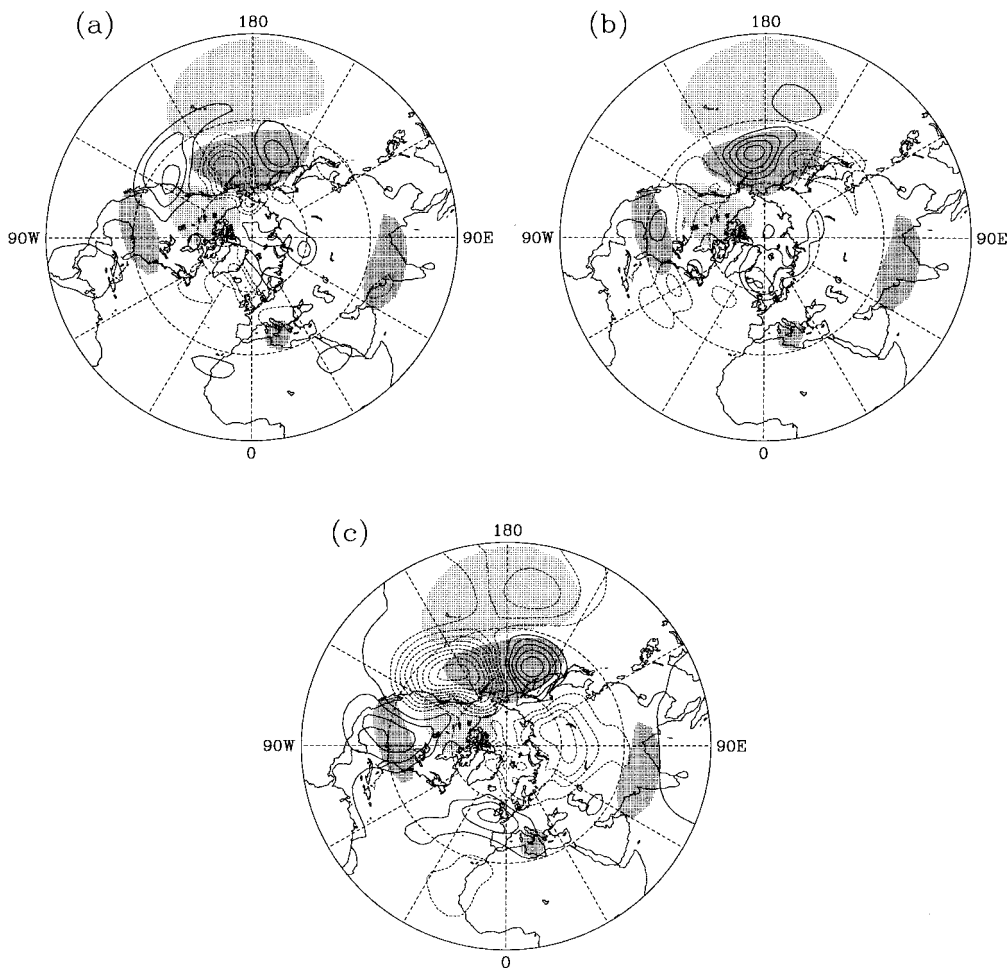


Figure 6. Composites at lag +6 days for various terms on the right-hand side of Eq. (2); (a) ξ_5 , (b) ξ_6 , and (c) ξ_4 (see text). The contour interval is $10.0 \text{ m}^2 \text{ s}^{-2}$ in (a) and (b) and is $25.0 \text{ m}^2 \text{ s}^{-2}$ in (c). Dashed contours are negative, and the zero contour is omitted. Dense (light) stippling indicates positive (negative) values of the daily unfiltered first rotated empirical orthogonal function.

–6 days to lag +2 days, this projection in the North Pacific is positive, and from lag +2 to lag +10 days this projection is negative, as illustrated in Fig. 6(a).

As discussed in section 3, for the negative phase, after completing much of its decay, the PNA index remains at about 30% of its peak value for about 10 days. Inspection of the projections in Fig. 3 reveals that to a large extent this is attributable to ξ_6 , the driving by the high-frequency transient eddies. Compared with the positive phase, an examination of ξ_6 for the negative phase (not shown) verifies that it has a spatial pattern very much like that for the positive phase, but of opposite sign, and that this particular spatial pattern persists for a much longer period of time. However, no explanation for this negative phase prolongation of ξ_6 is offered.

Amongst the linear terms during the PNA decay, ξ_1 , ξ_2 , and ξ_3 , retain the same spatial structure as during the PNA growth. On the other hand, the divergence term, ξ_4 , exhibits more substantial changes between the growth and decay phases (compare Fig. 5(f) with Fig. 6(c), which correspond to lag –2 and lag +6 days, respectively).

The negative ξ_4 projection onto the North Pacific stream-function anomaly strengthens, as does the positive ξ_4 projection onto the same anomaly. Furthermore, a region of negative ξ_4 develops which coincides with the negative stream-function anomaly in the subtropical Pacific. All of these changes result in a similar projection by ξ_4 at lag +6 days as at lag -2 days. When the ξ_4 projection is largest, at approximately lag +2 days, it also includes a dipole structure that overlaps with the North Pacific stream-function anomaly. The ξ_4 projection is largest at this lag because the negative contribution to this ξ_4 dipole has a magnitude of about twice that of the positive contribution, and because there is no subtropical Pacific contribution to ξ_4 (not shown). At the earliest stages of the anomaly growth, ξ_4 takes on a very different spatial structure (not shown). This is to be expected, given that the projection onto REOF1 in Fig. 2(c) is positive at these negative lags. This suggests that the divergence term may play a very different role during the PNA anomaly growth compared with that during the PNA anomaly decay. However, given that the barotropic model results of the following section show that a large fraction of the PNA anomaly growth is through the stationary advection term, it is likely that the divergence term plays only a secondary role during the anomaly growth.

The specification of terms on the r.h.s. of (2) does not allow one to address the question of whether the Rossby-wave source, i.e. the advection of the climatological absolute vorticity by the anomalous divergent wind (Sardeshmukh and Hoskins 1988), plays an important role in the life cycle of the PNA. Sardeshmukh and Hoskins (1988) showed that the midlatitude circulation can be influenced by tropical convection through the Rossby-wave source term. This particular term is calculated (not shown) and it is found that its maximum amplitude is substantially smaller than other terms on the r.h.s. of (2), and it has a spatial structure consistent with its being associated with the secondary circulation, i.e. it appears to be induced by midlatitude vorticity advection (see section 7(d)). These properties all suggest that anomalous tropical convection may not be very important during the PNA life cycle. A strong hint of this can be seen in Figs. 5(f) and 6(c), which show the inverse Laplacian of the anomalous divergence term. As this term is expected to resemble the anomalous velocity potential, it implies that the anomalous divergent wind out of the deep tropics is rather weak. Nevertheless, even though the Rossby-wave source term is small, it can still play an important role by exciting a small-amplitude anomaly which then grows barotropically to a large amplitude after propagating into the jet exit region.

7. BAROTROPIC MODEL RESULTS

Further insight into the PNA evolution can be obtained from integrating the forced, nonlinear, barotropic vorticity equation on the sphere. This equation can be written as

$$\frac{\partial \nabla^2 \psi'}{\partial t} + \{J(\psi', \nabla^2 \bar{\psi} + f) + J(\bar{\psi}, \nabla^2 \psi') + J(\psi', \nabla^2 \psi')\} = -\nu \nabla^{10} \psi' + F, \quad (8)$$

where ψ' is a stream-function anomaly, $\bar{\psi}$ the November to March climatological stream function, f the Coriolis parameter, J the Jacobian operator, ν the horizontal diffusion coefficient, and F is an external forcing term. The horizontal diffusion is used to parametrize the enstrophy cascade to subgrid scales. We can relate (8) to the Laplacian of (2) by matching the linear Jacobian terms in (8) with the first three linear terms in (2), i.e. $\sum_{i=1}^3 \xi_i$, the nonlinear Jacobian term in (8) with the self interaction contribution to ξ_5 , and F with $\sum_{i=4}^6 \xi_i + R$, i.e. the divergence term, the incoherent low-frequency advection term, the high-frequency forcing term, and the residual, respectively (with

this definition of R , the cross-frequency vorticity flux and tilting terms, i.e. ξ_7 and ξ_8 , are included in the residual).

For this model calculation, rhomboidal 30 resolution is used, the same as that in the diagnostic calculations. Also, the value chosen for ν is $8 \times 10^{37} \text{ m}^8 \text{ s}^{-1}$. Furthermore, only the results for the positive phase are illustrated, as all of the essential features to be presented are also found for the negative phase. For the initial stream-function field, the composite stream-function anomaly at a particular lag will be used. Composite values are also used for the forcing term F . Because the NCEP/NCAR re-analysis data are not available for every model time step (the barotropic model uses 48 time steps per day, and the known values of F are for the daily lags corresponding to 00 UTC), the values of F at each intermediate time step are approximated by using linear interpolation.

The unavoidable use of interpolation to determine F at each intermediate time step results in some error in the forcing terms. These errors in F must cause the model and observed anomalies to diverge gradually over time. As we will see, it is found that the model integrations are reasonably accurate when integrated over several days. However, for much longer model integrations, such as 10 days, noticeable differences between the model and observed anomalies were found.

(a) Growth stage

First the results of barotropic model integrations starting at lag -4 days are examined. The time period encompassing this model integration will be referred to as the growth stage. The extent to which this model simulates the PNA growth can be seen by comparing Fig. 4(b), i.e. the lag 0 composite anomalous stream-function field, with Fig. 7(f), the model run with all three forcing terms and the residual present. This comparison shows there is a large degree of similarity, especially in the region where the PNA has a large contribution. Figures 7(a) and 7(b) illustrate the results of the unforced linear and unforced nonlinear runs, respectively. In both of these runs, $F = 0$, and in the linear run the nonlinear Jacobian in (8) is set to zero. As can be seen, except for the slight westward displacement of the two Pacific anomalies in Fig. 7(b) relative to Fig. 7(a), these two runs yield extremely similar results, indicating that the nonlinear Jacobian in (8), which represents the self interaction term in (7), plays a very minor role. We can also see from Fig. 7(a) that substantial growth of the stream-function-anomaly pattern occurs in the linear unforced run (compare Fig. 7(a) with Fig. 4(a), which shows the initial flow for this calculation). Although not shown, inspection of the stationary advection term for the linear, unforced model run reveals a spatial pattern with two dominant anomalies over the North Pacific, as in Fig. 5(e). This suggests that the two upstream anomalies in the North Pacific grow via the stationary advection term, and implies that the two downstream anomalies grow via linear dispersion.

If we compare the locations of the stream-function anomaly centres in Fig. 7(a) with those of the corresponding observed composite stream-function anomaly in Fig. 4(b), we can see that the absence of the forcing terms in (8) leaves some noticeable errors in spatial structure. In particular, each of the model's anomaly centres is located to the east of the corresponding observed anomaly centre. Much of these differences are remedied by including the divergence term on the r.h.s. of (8) (Fig. 7(d)). In addition, for the two anomalies over the Pacific, the integration with the divergence term alone looks much more similar to that with all the forcing terms present (Fig. 7(f)) than those with just the high-frequency forcing (Fig. 7(c)) or the incoherent low-frequency advection forcing term (Fig. 7(e)), indicating that the divergence term has the most influence of the three forcing terms.

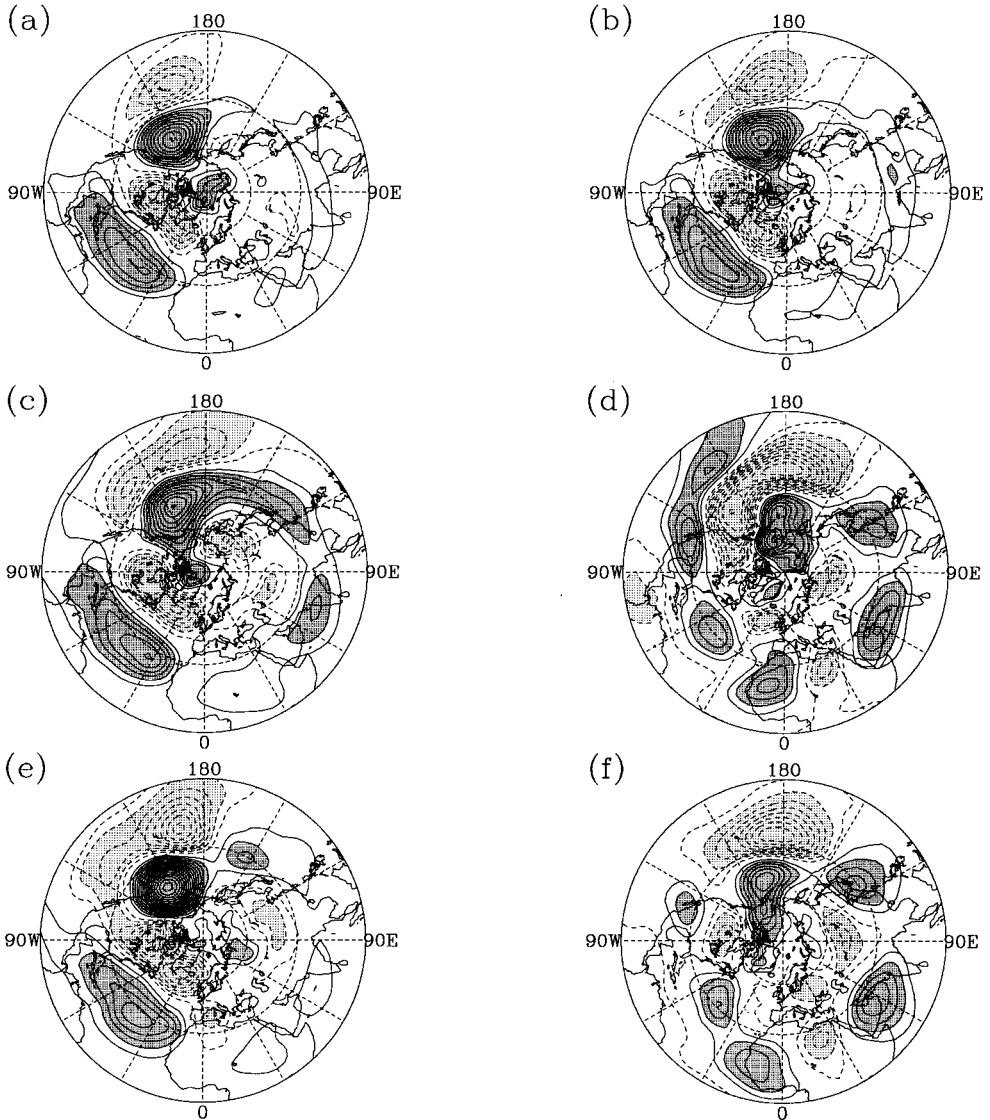


Figure 7. Anomalous stream-function field for the 4-day barotropic model integration. Start date is lag -4 days. The results shown are for (a) the unforced linear model, $J(\psi', \nabla^2 \psi') = 0$ and $F = 0$, (b) the unforced nonlinear model, $J(\psi', \nabla^2 \psi') \neq 0$ and $F = 0$, (c) the forced nonlinear model only with $\xi_6 \neq 0$, (d) the forced nonlinear model only with $\xi_4 \neq 0$, (e) the forced nonlinear model only with the incoherent contribution to $\xi_5 \neq 0$, and (f) the forced nonlinear model with ξ_4, ξ_5 , and ξ_6 all nonzero. The residual term, R , from Eq. (2), is also included amongst the forcing terms in (f). The contour interval is $2 \times 10^6 \text{ m}^2 \text{ s}^{-1}$. Dashed contours are negative, and the zero contour is omitted. Dense (light) stippling denotes positive (negative) values with a magnitude in excess of $4 \times 10^6 \text{ m}^2 \text{ s}^{-1}$. See text for explanation of terms.

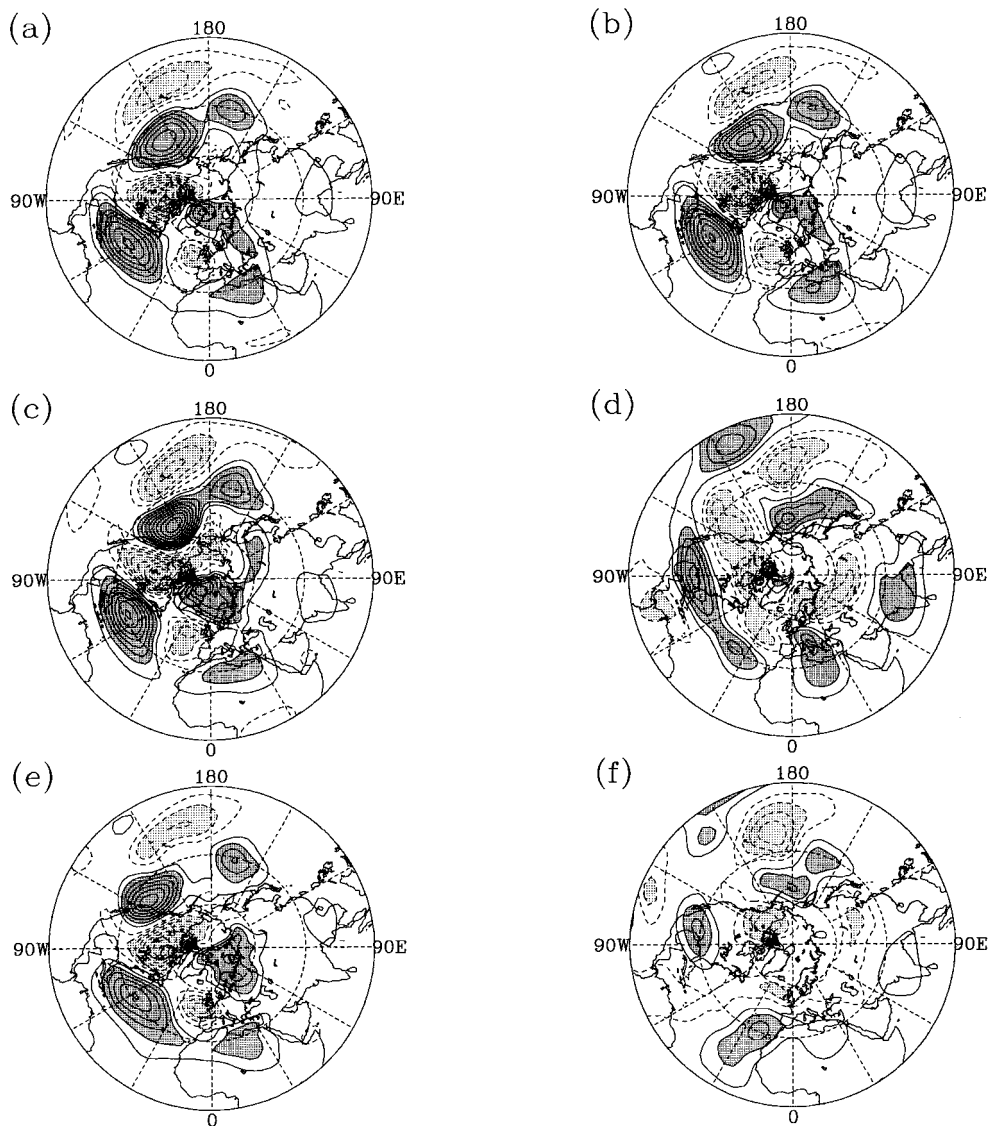


Figure 8. As Fig. 7, except with a start date of lag +4 days, and an integration time of 3 days.

(b) *Persistence stage*

The barotropic model results for an integration beginning on the onset day yield many of the same characteristics as those for the growth stage (not shown). The time period covered by this model integration is denoted as the persistence stage. As for the growth stage, the unforced linear and nonlinear runs yield very similar results. For these integrations, it is found that the subtropical stream-function anomaly decays very slightly, the North Pacific anomaly strengthens slightly, and the two downstream anomalies further amplify. Also, it is found that the divergence term is the most important of the three forcing terms. The divergence term again shifts the stream-function-anomaly centres upstream keeping them in a quasi-fixed position.

(c) *Decay stage*

Next the model integration beginning at lag +4 days is examined; the time period of this calculation is referred to as the decay stage (Fig. 8). However, in contrast to the previous stages, this integration is performed for only 3 days, as the stream-function anomaly in the model integration is found to diverge from the observed stream-function anomaly more rapidly during the decay stage. The degree to which the model integration simulates the PNA can be found by comparing Fig. 8(f), the model solution with all three forcing terms present, with the anomalous composite stream-function field at lag +7 days which, although not shown, is very similar to the stream-function field in Fig. 4(d), except for a slightly larger amplitude. As can be seen, the model integration does capture all four PNA anomaly centres reasonably well. As for the two previous stages, the linear and nonlinear unforced runs give very similar results (Figs. 8(a) and 8(b)). The two upstream stream-function anomalies decay while the two downstream anomalies continue to grow (compare with the initial flow shown in Fig. 4(c)). In contrast to the integrations for the two previous stages, during the decay stage the forcing terms have a much greater influence and, as can be seen, cause the stream-function anomaly to undergo substantial decay (Fig. 8(f)). Thus, because the stream-function-anomaly centres are retained in the unforced model runs, and yet decay in the fully forced model run (Fig. 8(f)), this result suggests that the decay of the PNA is not through linear dispersion. Also, as during the growth and persistence stages, the divergence term is the most important of the forcing terms (see Figs. 8(c) to 8(f)), although the incoherent low-frequency advection term is also playing an important role in the anomaly decay.

Although, as discussed in the above paragraph, linear dispersion does not seem to account for the overall decay of the PNA anomaly pattern, the unforced linear model results shown in Fig. 8(a) are consistent with linear dispersion weakening (strengthening) the upstream (downstream) stream-function-anomaly centres. This contrasts the unforced linear model results for the growth and persistence stages, as described above, where upstream anomaly growth was obtained. Since the background flow is identical in each integration, these differences in the unforced linear integrations must be due to changes in the spatial structure of the stream-function anomalies. (An examination of why the anomalies do change their shape is beyond the scope of this study.) Thus, since the projections, composite plots, and model integrations all suggest that the PNA grows via the energy gained through stationary advection, a linear process, it must be because of these changes in the spatial structure of the stream-function anomalies that the barotropic growth of the upstream anomaly centres eventually ceases.

(d) *Ekman pumping*

There are several plausible mechanisms that may account for the decay of the PNA. A list of mechanisms would include decay through anomalous Ekman pumping, thermal advection, and diabatic heating. Although the results to be presented below are not definitive, they do hint at an important role for Ekman pumping, as different variables show characteristics that are consistent with anomaly decay via Ekman pumping.

In order to estimate the influence of Ekman pumping, the divergence term, ξ_4 , is separated into two parts, i.e.

$$\xi_4 = - \sum_{i=1, i \neq 4}^8 \alpha \xi_i + \xi_{4ek}. \quad (9)$$

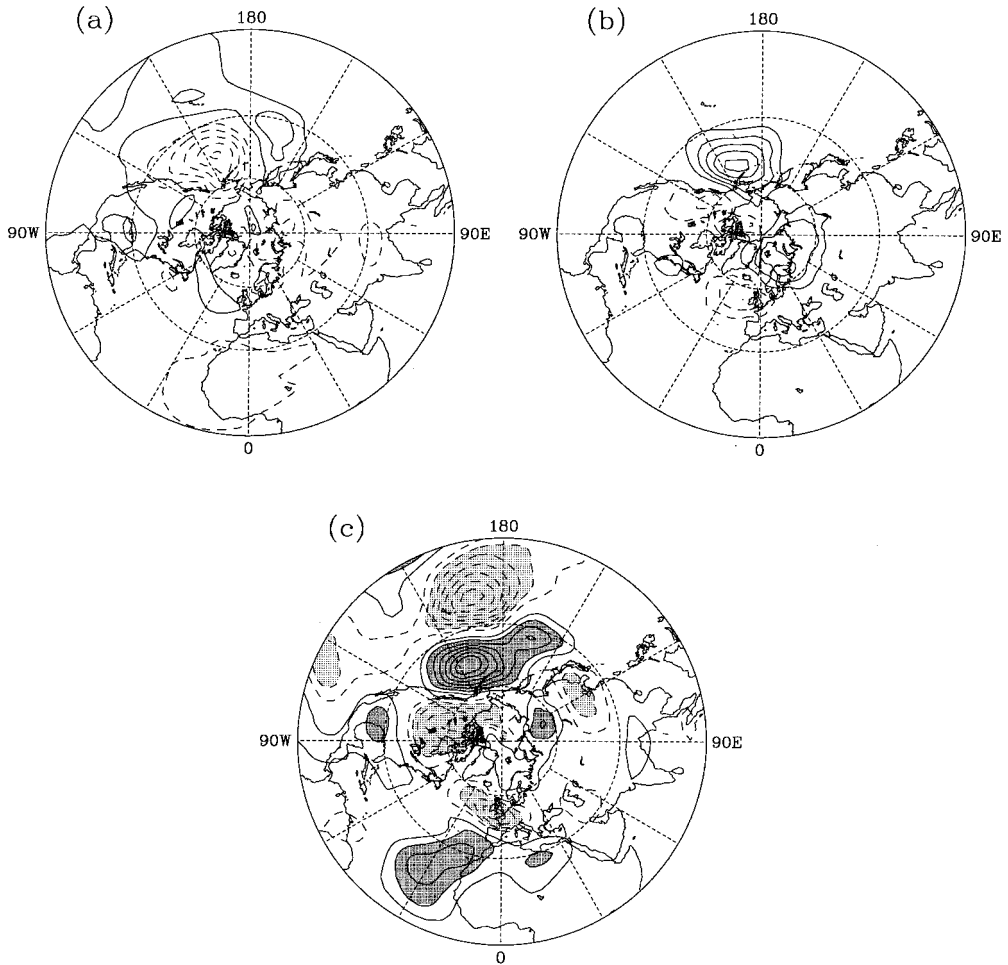


Figure 9. The lag +6 day (a) stream-function tendency due to the anomalous 'Ekman' divergence, ξ_{4ek} , and (b) anomalous surface pressure. (c) The anomalous stream-function field from the barotropic model integration for the decay stage with the anomalous 'Ekman' divergence set to zero. The contour intervals are (a) $10.0 \text{ m}^2\text{s}^{-2}$, (b) 150 N m^{-2} , and (c) $2 \times 10^6 \text{ m}^2\text{s}^{-1}$. Dashed contours are negative, and the zero contour is omitted. Dense (light) stippling in (c) denotes positive (negative) values with a magnitude in excess of $4 \times 10^6 \text{ m}^2\text{s}^{-1}$.

The first term on the r.h.s. of (9) represents the divergence associated with the secondary circulation due to upper-tropospheric vorticity advection. This term simply represents the adjustment of the flow toward thermal-wind balance due to the anomalous vorticity advection. The parameter α , which is a measure of the strength of the secondary circulation, must have a magnitude less than unity, as the secondary circulation always acts to weaken the influence of the processes that drives it. After specifying α , the second term on the r.h.s. of (9) can be determined. Physically, ξ_{4ek} can be induced by thermal advection, diabatic heating, and friction (e.g. Ekman pumping), as mentioned above, and also by that part of vorticity advection not captured by the first term on the r.h.s. of (9). Also, although it is of course impossible to show with complete confidence that ξ_{4ek} does indeed correspond to the influence of Ekman pumping, by showing that the spatial structure of ξ_{4ek} is consistent with that expected for Ekman pumping, one can argue qualitatively that PNA decay through Ekman pumping is indeed plausible.

In order for surface friction to influence the 300 mb stream-function anomaly, the anomalous vertical circulation driven by Ekman pumping must be deep, i.e. extend through the depth of the troposphere. Furthermore, Ekman pumping requires that ξ_{4ek} takes on specific characteristics. These include that ξ_{4ek} should be similar in spatial structure but opposite in sign to both (a) the 300 mb stream-function anomaly, and (b) the surface pressure anomaly. The first requirement is necessary simply because ξ_{4ek} must be damping the stream-function anomaly. The second point, which links the stream-function anomaly to the surface circulation where friction is generated, needs further discussion. Because the influence of surface friction requires a deep anomalous vertical circulation, the sign of the divergence anomaly in the upper troposphere that results from Ekman pumping must be opposite to that for the divergence anomaly near the surface. Furthermore, at the surface, a positive (negative) pressure anomaly always coincides with a positive (negative) divergence anomaly, via downgradient cross-isobaric flow. Thus, combining these properties, upper-tropospheric convergence, i.e. a negative ξ_{4ek} , must coincide with a positive surface pressure anomaly.

The approach adopted is to vary α and examine if for a range of α values whether the two requirements of the above paragraph are satisfied. Figure 9(a), shows ξ_{4ek} estimated from (9) using $\alpha = 0.6$. The anomalous surface pressure field is illustrated in Fig. 9(b). Both of these fields are illustrated at lag +6 days, a time when the stream-function anomaly is rapidly decaying. As can be seen, the two requirements of the above paragraph are indeed satisfied, since ξ_{4ek} (Fig. 9(a)) and the anomalous surface pressure field (Fig. 9(b)) both closely resemble the positive stream-function anomaly in the North Pacific (Fig. 4(b) and 4(c)). Thus, keeping in mind the assumptions made and the qualitative nature of these calculations, these findings are consistent with the hypothesis that the PNA is decaying through frictional processes via Ekman pumping.

Further support for the role of Ekman pumping in the decay of the PNA can be obtained by integrating the barotropic model with the 'Ekman pumping contribution' to the divergence set equal to zero, and with the same initial flow as that corresponding to Fig. 8. When this integration is performed (Fig. 9(c)), it can be seen that the stream-function anomalies decay only slightly, and that the PNA is mostly retained.

8. CONCLUSIONS

This study investigates some of the dynamical mechanisms associated with the growth and decay of the Pacific/North American teleconnection pattern (PNA). Through the use of projections, composites of various terms in the stream-function-tendency equation, a series of calculations with a forced, nonlinear, barotropic model, and a crude estimate of the role of Ekman pumping, a rather simple picture of PNA evolution is presented. The growth of the two upstream anomaly centres of the PNA is found to occur through barotropic energy conversion from the zonally asymmetric climatological flow. This is consistent with numerous other studies of low-frequency variability, e.g. Simmons *et al.* (1983). Dispersion then transfers energy to the two downstream anomaly centres. Divergence is found to be important, as it causes upstream anomaly propagation, which allows the two upstream anomaly centres to remain in a quasi-fixed position in the Asian jet exit region. However, as the PNA anomaly undergoes its life cycle, the horizontal shape of the two upstream anomalies gradually changes. This results in a reduction of the barotropic growth followed by decay of the PNA through Ekman pumping. This entire cycle is complete within approximately 2 weeks. It is important to emphasize that the above Ekman-pumping argument is only

qualitative, and does not rule out the possibility of baroclinic processes causing the decay of the PNA.

The above findings suggest that the PNA evolution is dominated by linear processes, as found by Feldstein (1998) for another anomaly pattern in a general-circulation model. However, at various stages during the PNA life cycle it was found that the nonlinear transient eddy fluxes can play an important role. Nevertheless, the overall dominance of the linear terms suggests that to lowest order the PNA life cycle has the characteristics of a linear initial-value problem.

Many studies of low-frequency variability have used barotropic models. However, by analysing the normal mode and optimal growth properties of the observed atmospheric flow, and also with the aid of stochastic modelling, a number of papers (Borges and Sardeshmukh 1995; Blade 1996; Sardeshmukh *et al.* 1997; Newman *et al.* 1997) have shown that barotropic processes alone cannot account for the temporal evolution of low-frequency anomalies. Furthermore, as the authors of these studies discuss, additional processes, such as baroclinic effects, i.e. divergence, diabatic heating, etc., and transient eddy forcing, must play a crucial role in the life cycle of low-frequency anomalies. The results of the present study provide additional support for these ideas.

ACKNOWLEDGEMENTS

This research was supported by the National Science Foundation through Grants ATM-9712834 and ATM-0003039. I would like to thank Dr Sukyoung Lee for her beneficial discussions, and also two anonymous reviewers. In addition, I would like to thank the National Oceanic and Atmospheric Administration Climate Diagnostics Center for providing me with the NCEP/NCAR reanalysis dataset.

REFERENCES

- | | | |
|--------------------------------------|------|---|
| Barnston, A. G. and Livezey, R. E. | 1987 | Classification, seasonality, and persistence of low-frequency atmospheric circulation patterns. <i>Mon. Weather Rev.</i> , 115 , 1083–1126 |
| Black, R. X. and Dole, R. M. | 1993 | The dynamics of large-scale cyclogenesis over the North Pacific Ocean. <i>J. Atmos. Sci.</i> , 50 , 421–442 |
| Blade, I. | 1996 | On the relationship of barotropic singular modes to the low-frequency variability of a general circulation model. <i>J. Atmos. Sci.</i> , 53 , 2393–2399 |
| Borges, M. D. and Sardeshmukh, P. D. | 1995 | Barotropic Rossby wave dynamics of zonally varying upper-level flows during northern winter. <i>J. Atmos. Sci.</i> , 52 , 3779–3796 |
| Branstator, G. | 1984 | The relationship between the zonal mean flow and quasi-stationary waves in the midtroposphere. <i>J. Atmos. Sci.</i> , 41 , 2163–2178 |
| | 1987 | A striking example of the atmosphere's leading traveling pattern. <i>J. Atmos. Sci.</i> , 44 , 2310–2323 |
| | 1990 | Low-frequency patterns induced by stationary waves. <i>J. Atmos. Sci.</i> , 47 , 629–648 |
| | 1992 | The maintenance of low-frequency atmospheric anomalies. <i>J. Atmos. Sci.</i> , 49 , 1924–1945 |
| Cai, M. and van den Dool, H. M. | 1994 | Dynamical decomposition of low-frequency tendencies. <i>J. Atmos. Sci.</i> , 51 , 2086–2100 |
| Cash, B. A. and Lee, S. | 2000 | Dynamical process of block evolution. <i>J. Atmos. Sci.</i> , 57 , 3202–3218 |
| | 2001 | Observed nonmodal growth of the Pacific–North American teleconnection pattern. <i>J. Climate</i> , 14 , 1017–1028 |
| Dole, R. M. and Black, R. X. | 1990 | Life cycles of persistent anomalies. Part II: The development of persistent negative height anomalies over the North Pacific Ocean. <i>Mon. Weather Rev.</i> , 118 , 824–846 |
| Egger, J. and Schilling, H.-D. | 1983 | On the theory of the long-term variability of the atmosphere. <i>J. Atmos. Sci.</i> , 40 , 1073–1085 |

- Feldstein, S. B. 1998 The growth and decay of low-frequency anomalies in a GCM. *J. Atmos. Sci.*, **55**, 415–428
- 2000 The time-scale, power spectra, and climate noise properties of teleconnection patterns. *J. Climate*, **13**, 4430–4440
- Feldstein, S. B. and Lee, S. 1996 Mechanisms of zonal index variability in an aquaplanet GCM. *J. Atmos. Sci.*, **53**, 3541–3555
- Franzke, C., Fraedrich, K. and Lunkeit, F. 2001 Teleconnections and low-frequency variability in idealized experiments with two storm tracks. *Q. J. R. Meteorol. Soc.*, **127**, 1321–1339
- Frederiksen, J. S. 1983 A unified three-dimensional instability theory of the onset of blocking and cyclogenesis. II: Teleconnection patterns. *J. Atmos. Sci.*, **40**, 2593–2609
- Holton, J. R. 1992 *An introduction to dynamic meteorology*. Academic Press, San Diego, USA
- Horel, J. D. 1985 Persistence of the 500 mb height field during northern hemisphere winter. *Mon. Weather Rev.*, **113**, 2030–2042
- Hoskins, B. J. and Karoly, D. 1981 The steady linear response of a spherical atmosphere to thermal and orographic forcing. *J. Atmos. Sci.*, **38**, 1179–1196
- Hoskins, B. J., James, I. N. and White, G. H. 1983 The shape, propagation, and mean-flow interaction of large-scale weather systems. *J. Atmos. Sci.*, **40**, 1595–1612
- Kang, I.-S. 1990 Influence of zonal mean flow change on stationary wave fluctuations. *J. Atmos. Sci.*, **47**, 141–147
- Kushnir, Y. 1987 Retrograding wintertime low-frequency disturbances over the North Pacific Ocean. *J. Atmos. Sci.*, **44**, 2727–2742
- Kushnir, Y. and Wallace, J. M. 1989 Low-frequency variability in the northern hemisphere winter: Geographical distribution, structure and time-scale dependence. *J. Atmos. Sci.*, **46**, 3122–3142
- Lau, N.-C. 1988 Variability of the observed midlatitude storm tracks in relation to low-frequency changes in the circulation pattern. *J. Atmos. Sci.*, **45**, 2718–2743
- Livezey, R. E. and Chen, W. Y. 1983 Statistical field significance and its determination by Monte Carlo techniques. *Mon. Weather Rev.*, **115**, 46–59
- Mo, K. C. 1986 Quasi-stationary states in the southern hemisphere. *Mon. Weather Rev.*, **114**, 806–823
- Newman, M., Sardeshmukh, P. D. and Penland, C. 1997 Stochastic forcing of the wintertime extratropical flow. *J. Atmos. Sci.*, **54**, 435–455
- Nigam, S. and Lindzen, R. S. 1989 The sensitivity of stationary waves to variations in the basic state zonal flow. *J. Atmos. Sci.*, **46**, 1746–1768
- Sardeshmukh, P. D. and Hoskins, B. J. 1988 The generation of global rotational flow by steady idealized tropical divergence. *J. Atmos. Sci.*, **45**, 1228–1251
- Sardeshmukh, P. D., Newman, M. and Borges, M. D. 1997 Free barotropic Rossby wave dynamics of the wintertime low-frequency flow. *J. Atmos. Sci.*, **54**, 5–23
- Simmons, A. J., Wallace, J. M. and Branstator, G. 1983 Barotropic wave propagation and instability and atmospheric teleconnection patterns. *J. Atmos. Sci.*, **40**, 1363–1392
- Ting, M. and Lau, N.-C. 1993 A diagnostic and modeling study of the monthly mean wintertime anomalies appearing in an 100-year GCM experiment. *J. Atmos. Sci.*, **50**, 2845–2867
- Wallace, J. M. and Gutzler, D. S. 1981 Teleconnections in the geopotential height field during the northern hemisphere winter. *Mon. Weather Rev.*, **109**, 784–812